Identification and validation of an extended Stewart-Cazacu micromechanics damage model applied to Ti–6Al–4V specimens exhibiting positive stress triaxialities

Carlos Rojas-Ulloa[1]; Marian Valenzuela[2,3]; Víctor Tuninetti[1,*]; Anne-Marie Habraken[4]

[1] Department of Mechanical Engineering, Universidad de La Frontera, Francisco Salazar 01145, Temuco 4780000, Chile

[2] Department of Civil Engineering and Geology, Universidad Católica de Temuco, Rudecindo Ortega 02950, 4780000 Temuco, Chile

[3] Doctoral Program in Sciences of Natural Resources, Universidad de La Frontera, Temuco, Chile

[4] ArGEnCo Department, MSM team, University of Liège, Quartier POLYTECH 1, allée de la Découverte 9, Liège 4000, Belgium

*Corresponding author: victor.tuninetti@ufrontera.cl; tel.: + 56452325984.

Abstract

In this research, the Stewart-Cazacu micromechanics coupled damage model is extended and validated adding nucleation and coalescence models as new damage mechanisms. The Ti–6Al–4V titanium alloy is chosen as a suitable hcp ductile material to be modeled using this extended damage law. The characterization of the damage evolution in this alloy is addressed throughout a quasi-static experimental campaign. Damage characterization relies on in-situ X-ray tomography data and Scanning Electron Microscopy (SEM) imaging technique. The validation procedure consists in the implementation into the finite element (FE) research software Lagamine of ULiège and in the comparison of numerical predictions and experimental results. Load-displacement curves and damage related state variables at fracture configuration from smooth and notched bar specimens submitted to tensile tests are analyzed. The nucleation and coalescence model extensions as well as an accurate elastoplastic and damage material parameter identification for Ti–6Al–4V samples are essential features to reach a validated model. The prediction capabilities exhibited for large strains are in good agreement with experimental results, while the near-fracture strains can still be improved.

Keywords

Finite element modeling; Micromechanics damage model; Cazacu yield criterion; ductile fracture; hcp material

1. Introduction

Ductile fracture is known to be the result of the growth, nucleation and ultimate coalescence of microcavities driven by plastic deformation.[1–4] Furthermore, the continuous increment of damage along large and near-fracture deformation states affects the overall mechanical response of the material, causing a reduction of the supported load in comparison with a non-porous material. The consideration of damage during certain metal forming processes, such as bending, single point incremental forming (SPIF) or deep drawing, [5–9] is essential for correctly predicting the mechanical behavior and failure of the material.

Based in the CPB06 yield criterion,[10–16] a micromechanics mathematical approach carried out by J. Stewart and O. Cazacu resulted in the development of the SC11 damage law.[11,17] This damage law is suitable for porous ductile metallic materials with hcp crystalline structure that exhibit orthotropy and strength differential (SD) effect. Damage is modeled in the form of void growth and allows predicting distortional hardening (DH) behavior and material softening by reducing the updated yield surface of the material along large and near-fracture strains.

Due to their exceptional mechanical properties, titanium alloys have been a fundamental component in a wide variety of engineering solutions and critical applications.[18,19] The Ti–6Al–4V is currently the most widely used titanium alloy in the world.[20] The relatively high cost of this alloy is compensated by its high strength to weight ratio, high corrosion resistance, weldability and biocompatibility. Ti–6Al–4V is present in a wide variety of key components in aeronautical, automotive, military and biomedical industries.[20–25] Its crystalline structure at room temperature consists in a combination of two main phases : primary $(\alpha - \mathrm{Ti})$ structure, composed of hexagonal closed plackets crystals (hcp), and secondary $(\beta - \mathrm{Ti})$ structure, based on body centered cube crystals (bcc).[26] The experimentally observed mechanical behavior of this titanium alloy is complex, exhibiting orthotropy, SD effect and DH effect.[12–14,27,28] FE simulations using the CPB06 yield criterion has been chosen for modeling Ti–6Al–4V mechanical behavior along large strains.[10] However, when near-fracture strains are reached, the DH effects are observed as an irregular evolution of the Ti–6Al–4V yield locus. In order to correctly predict near-fracture stress states, a series of different yield surfaces were identified at different plastic work levels, while the current yield surface of the material is calculated by linear interpolation technique.[12–14,27] Although this method has proven to be accurate enough, its approach is based in a phenomenological depiction of a physical phenomenon. The SC11—TN micromechanics damage law extends the CPB06 formulation, based on the continuum modeling of a porous material. It assumes that the yield stress of the material is affected by number and size of cavities (pores) within the material.

Several articles focused in micromechanics behavior of Ti–6Al–4V present valuable information related to the damage evolution and its effect on the mechanical behavior and ductile fracture of Ti–6Al–4V.[29–33] Nucleation, growth and coalescence of micro-voids are characteristics of the damage mechanisms for positive stress triaxialities.[1,2,8,34–39] Very low positive or negative stress triaxialities such as in pure shear and compression loads exhibit other predominant damage mechanisms such as the formation, rotation and enlarging of shear induced micro-cracks.[40] In this work, the identification and validation of the SC11—TN extended damage model on smooth and notched Ti–6Al–4V bars with positive stress triaxiality loadings are presented. A micromechanics characterization of the damage evolution has been performed by an in-situ X-ray tomography imaging technique[31] in conjunction with a new SEM image sampling over critical zones within Ti–6Al–4V sample submitted to near-fracture strains. These data were used to identify the ongoing damage mechanisms and the damage material parameters.

2. Formulation of SC11—TN damage law

Based on continuum mechanics principles, the analytical formulation of SC11 damage law is presented in Equation 1. It is generated from a continuum macroscopic extrapolation of a micromechanics analysis of an hcp metallic material cell surrounding a spherical hollow void.[11,17] The yield locus is defined by:

$$\Phi(\boldsymbol{\sigma}, \bar{\epsilon}^p) = \left[\frac{\bar{\Sigma}_{\mathrm{CPB06}}}{\sigma_y}\right]^2 + 2q_1 D cosh\left[\frac{3q_2(\Sigma_m - X_m)}{h\sigma_y}\right] - 1 - q_3 D^2 = 0 \qquad (1)$$

where $\bar{\Sigma}_{\mathrm{CPB06}}$ is the macroscopic CPB06 yield stress, σ_y is the current yield stress calculated through a defined isotropic hardening law, Σ_m and X_m are respectively the hydrostatic components of the corrected stress and backstress tensors, h is the hydrostatic coefficient, D is the total porosity ratio and q_i are parameters proposed by Refs.[17,37,41] for adjusting the damage evolution to account for the effects of non-spherical voids evolution.

The CPB06 equivalent stress is calculated as:

$$\bar{\Sigma}_{CPB06} = \tilde{m}\left\{\sum_{i=1}^{3}[(\Sigma_i - \mathrm{X}_i) - k|\Sigma_i - \mathrm{X}_i|]^a\right\}^{\frac{1}{a}} \tag{2}$$

where Σ_i and X_i are respectively the eigenvalues of the corrected deviatoric stress tensor defined through material orthotropic parameters and the backstress tensor defined by the Armstrong-Frederick kinematic hardening law.[42] k is the asymmetry parameter for accounting the SD effect, a is the degree of homogeneity, and $\tilde{m}$ is a constant that transforms the CPB06 equivalent stress into the CPB06 yield stress in the direction where the isotropic hardening law was identified, i.e., the direction where the yield stress σ_y is calculated. While the backstress tensor is calculated by means of a properly defined kinematic hardening law, the eigenvalues of the corrected stress tensor are calculated from the stress tensor as shown in Equation 3:

$$\Sigma_i = \left(L_{ijmn}T_{mnkl}\sigma_{kl}\right)_{ii} \tag{3}$$

where L_{ijmn} is the 4th order tensor of material orthotropic parameters defined in Cazacu law,[10] T_{mnkl} is the 4th symmetric deviatoric unit transformation tensor, and σ_{kl} is the stress tensor. The symmetric 4th order tensor of material orthotropic constants is presented in Voigt notation in Equation 4:

$$\mathbf{L} = \begin{pmatrix} L_{11} & L_{12} & L_{13} & 0 & 0 & 0 \\ L_{12} & L_{22} & L_{23} & 0 & 0 & 0 \\ L_{13} & L_{23} & L_{33} & 0 & 0 & 0 \\ 0 & 0 & 0 & L_{44} & 0 & 0 \\ 0 & 0 & 0 & 0 & L_{55} & 0 \\ 0 & 0 & 0 & 0 & 0 & L_{66} \end{pmatrix} \tag{4}$$

In its original form, SC11 considers the total porosity ratio to be the result of only the growth of voids initially contained within the matrix material. The growth of voids is known to be the consequence of the volumetric component of the velocity gradient, and is highly related to the triaxiality. The phenomenological growth model is presented in Equation 5, where $\dot{f}_g$ is the increment rate of the porosity ratio due to voids growth and $\dot{\boldsymbol{\epsilon}}^{\mathbf{p}}$ is the plastic strain rate tensor of the continuum damage model. This incremental void growth formulation has been widely used and accepted for a variety of coupled damage laws.[35,37,41]

$$\dot{f}_g \approx (1 - q_1 D) tr(\dot{\boldsymbol{\epsilon}}^{\mathbf{p}}) \tag{5}$$

In order to include the nucleation and coalescence of voids as damage mechanisms within this damage law, the phenomenological nucleation and coalescence models of Tvergaard & Needleman are implemented.[41] Hence resulting in the SC11—TN extended damage model, where the total porosity ratio D is considered to be the result of growth, nucleation and coalescence of voids. The mathematical formulation for modeling the nucleation of voids is given in Equation 6, following a macroscopic statistical approach acknowledging a normal distribution in the onset of voids,[4] where F_{N}, S_{N} and ϵ_{N} are the material parameters.

$$\dot{f}_n = \frac{F_{\mathrm{N}}}{S_{\mathrm{N}}\sqrt{2\pi}} \exp\left[-\frac{1}{2}\left(\frac{\bar{\epsilon}^p - \epsilon_{\mathrm{N}}}{S_{\mathrm{N}}}\right)^2\right] \dot{\bar{\epsilon}}^p \tag{6}$$

The coalescence of cavities is modeled as an increment in the slope of the porosity ratio curve ruled by Equation 7, where f_U is the ultimate porosity ratio, f_F is the fracture porosity ratio and f_{cr} is the critical porosity ratio defining the threshold to start coalescence.

$$D = \begin{cases} f = f_g + f_n & if \quad f \leq f_{cr} \\ f_{cr} + \frac{(f_U - f_{cr})(f - f_{cr})}{f_F - f_{cr}} & if \quad f > f_{cr} \end{cases} \qquad (7)$$

The statistical approach for modeling nucleation of voids is graphically explained in Figure 1 (a), while the relation between coalescence parameters and total porosity ratio evolution is given in Figure 1 (b).

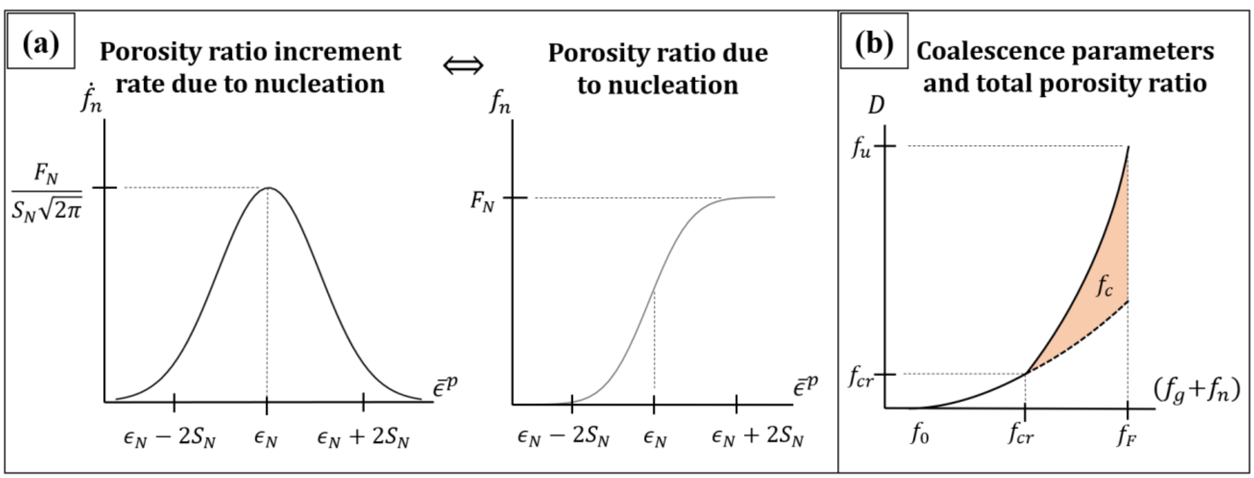

Figure 1. (a) Graphical representation of normal distribution nucleation model and related parameters in incremental and total configuration. **(b)** Schematic of relation between coalescence model parameters and total porosity ratio.

2. Material and methods

2.1. Material

The quasi-static elastoplastic characterization of this particular bulk sample of Ti–6Al–4V is provided by Tuninetti et al.[13,14] As an α/β- titanium alloy exhibiting orthotropy and SD effect, this earlier identification procedure considered the CPB06 yield criterion (i.e., SC11—TN without damage) in conjunction with the Voce's isotropic hardening law for modeling the plastic behavior of the material, whereas the elastic behavior was modeled throughout the Hooke's law. The posterior simulations based in the CPB06 law were able to predict the tensile plastic instability and post-necking hardening of Ti–6Al–4V. The Voce's isotropic hardening law defining the yield stress in function of the equivalent plastic strain $\bar{\epsilon}^p$ is given by Equation 8.

$$\sigma_y(\bar{\epsilon}^p) = A_0 + B_0[1 - \exp(-C_0\bar{\epsilon}^p)] \tag{8}$$

The elastoplastic parameters identified by Tuninetti et al.[14] and Guzman et al.[43] presented in Table 1, are hereafter used for modeling both yield locus and hardening of Ti–6Al–4V. The (1,2,3) orthotropic material frame was identified from a pristine ingot sample, and is defined as Longitudinal Direction (LD), Transversal Direction, and Short Transversal direction (ST). The parameters for the Voce's isotropic hardening law (Equation 8) were identified along the LD direction. This simplified identification strategy approach is the first step towards a more advanced characterization. In future work, a coupled identification of the damage-elasto-plastic laws should further increase the predictive capability of the model. Note also that the parameter set used here uses a mean orthotropic tensor L and assumes no DH, since at this early stage of the research, this feature is not yet implemented in SC11—TN.

Table 1. Identified material parameters describing the elastoplastic CPB06 and Voce models for Ti–6Al–4V.

<table>
<tr><th colspan="12">Elastic constants</th></tr>
<tr><td colspan="3">E_{11} (GPa)</td><td colspan="3">E_{22} (GPa)</td><td colspan="3">E_{33} (GPa)</td><td colspan="3">$\nu_{12} = \nu_{13} = \nu_{23}$</td></tr>
<tr><td colspan="3">112.0</td><td colspan="3">115.0</td><td colspan="3">117.0</td><td colspan="3">0.3</td></tr>
<tr><th colspan="12">Elastoplastic constants</th></tr>
<tr><td colspan="12">Components of the orthotropic constants tensor L</td></tr>
<tr><td>L_{11}</td><td>L_{12}</td><td>L_{13}</td><td>L_{22}</td><td>L_{23}</td><td>L_{33}</td><td colspan="6">$L_{44} = L_{55} = L_{66}$</td></tr>
<tr><td>1</td><td>-2.373</td><td>-2.364</td><td>-1.838</td><td>1.196</td><td>-2.444</td><td colspan="6">-3.607</td></tr>
<tr><td colspan="6">Asymmetry parameter $k = 0.113$</td><td colspan="6">Degree of homogeneity $a = 2.0$</td></tr>
<tr><td colspan="12">Voce’s isotropic hardening law parameters (Equation 8)</td></tr>
<tr><td colspan="4">A_0 (MPa)</td><td colspan="4">B_0 (MPa)</td><td colspan="4">C_0</td></tr>
<tr><td colspan="4">921.0</td><td colspan="4">290.0</td><td colspan="4">5.80</td></tr>
</table>

2.2. Damage and damage evolution analyses

The further execution of numerical simulations using the implemented SC11—TN damage law implies the characterization of damage and identification damage related parameters. With this in mind, two different experimental techniques were considered.

It is important to notice that all experimental tests considered in this work have been performed using the same Ti—Al—4V material batch.

2.2.1. In situ X-ray microtomography

This experimental procedure, performed by Lecarme et al.[31], aimed of quantifying the progressive evolution of the porosity ratio contained within a small volume located in a critical zone at the neck center of a Ti–6Al–4V notched bar specimen submitted to a tensile test. This was accomplished by the execution of an in-situ X-ray micro-tomography technique in conjunction with an advanced automatic void-tracking algorithm.[31] Technological limitations made impossible the accurate identification of coalescence, the measurement of near-fracture porosity ratio and the detection of voids smaller than the minimal pixel size of $1.06 \times 1.06 \times 1.06\ \mu m^3$.[31,44] Nevertheless, the retrieved data allow for the identification of the nucleation function parameters introduced in Equation 6 throughout a direct identification procedure.

2.2.2. Near-fracture SEM analysis

With the objective of recognizing near-fracture damage patterns, several SEM images were captured from a Ti–6Al–4V notched bar specimen submitted to a monotonic tensile test stopped near the fracture. The current axial deformation was monitored using a Zwick Multisens-extensometer, while the real-time notch shape was monitored with three systems of two-CCD cameras and Vic3D software for three-dimensional digital image correlation (DIC) technique. In order to obtain a non-fractured specimen subjected to a near-fracture tensile load, two control tensile tests were executed for determining the actual fracture force of the specimen. A third specimen was then submitted to a final tensile test until reaching the previously determined fracture force. Once unloaded, samples from the notch zone were obtained and polished for further SEM analysis. The post-processing of the SEM images also allowed to map the apparent porosity ratio (i.e., measured as surface ratio) along the axial and transversal planes of the notched bar.

2.3. Damage parameters identification procedure

Direct and inverse different identification techniques were used for identification of the damage parameters for the active damage mechanisms detected through the SEM analysis described above. A direct identification strategy was applied for identifying the initial porosity ratio f_0 for modeling the growth of initial voids. Based in the analysis and postprocessing of the total porosity ratio evolution results from Lecarme et.al.,[31]an inverse identification strategy was used for identifying the nucleation parameters. Finally, a combined direct-inverse identification procedure was carried out to identify the coalescence parameters.

2.4. Validation procedure

The validation procedure is addressed throughout a comparison between numerical and experimental tensile load-displacement curves. For this purpose, three different geometries of Ti–6Al–4V bar samples (Figure 2) aligned with the LD direction of the material, acknowledging positive triaxialities ranging from 1.0 to 1.75, were submitted to tensile tests. In particular, the experimental procedure considered three tensile tests per each geometry in order to obtain average curves with their respective standard deviations (St. Dev.). The simulations were performed using the FE research software Lagamine, where the actual SC11—TN coupled damage law has been implemented.

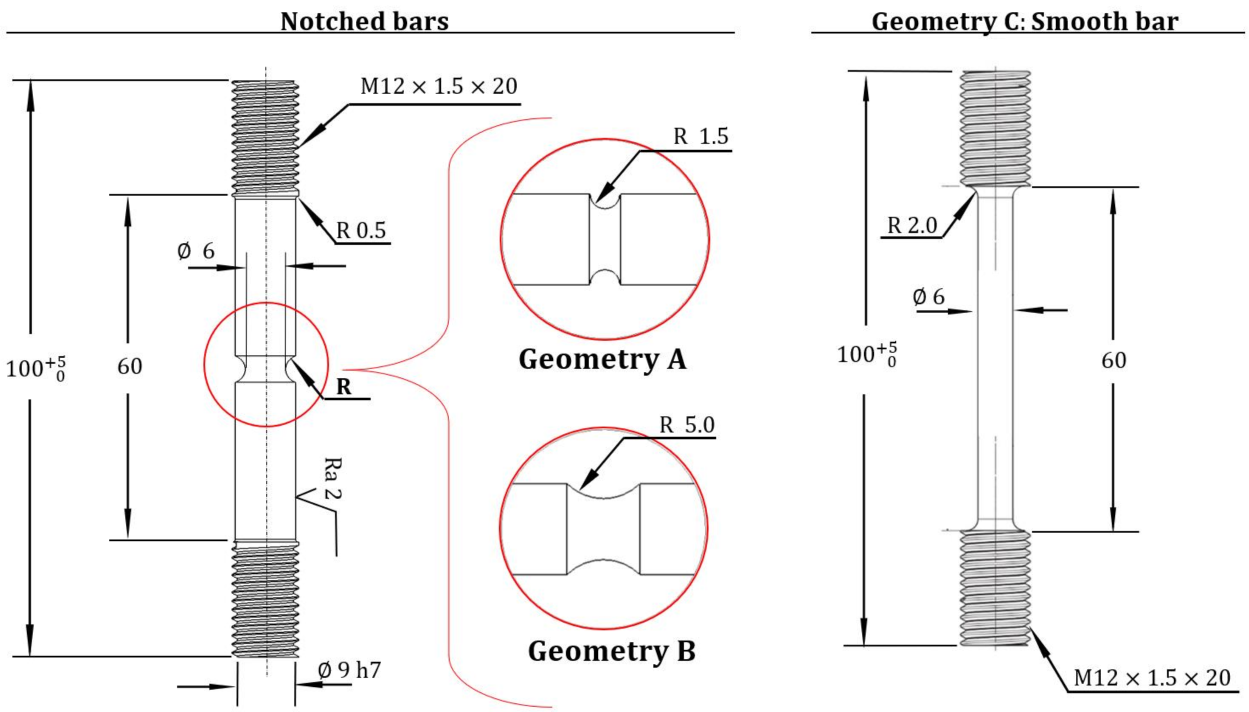

Figure 2. Ti–6Al–4V smooth and notched bar geometries used for the validation of SC11—TN continuum micromechanics damage model along with the identified parameters. Dimensions in millimeters.

The quasi-static experimental tensile tests were performed at a constant axial strain rate of $\dot{\epsilon} = 1 \times 10^{-3}$ (s^{-1}). Replicating the experimental procedure, this constant strain rate was applied to the FE simulated tensile tests until the experimentally observed onset of fracture.

3. Damage characterization

Since the elastoplastic CPB06 related parameters for Ti–6Al–4V are already given in Table 1, the identification procedures of damage related parameters for modeling growth, nucleation and coalescence of voids for SC11—TN is described in this section.

3.1. SEM experimental observations

The geometry of the Ti–6Al–4V notched bar submitted to a near-fracture tensile test is presented in Figure 3 (a). A simplified illustration of the shape and size of cavities due to the effect of the stress and deformation fields on the initial voids contained in the notch zone is shown in **Erreur ! Source du renvoi introuvable.** (b), while representative SEM images from axial and transversal planes are respectively shown in **Erreur ! Source du renvoi introuvable.** (c) and (d). In the context of a visual analysis in Erreur ! Source du renvoi introuvable. (c), the red dotted lines encircle the observed coalescence of primary voids, while the yellow dash lines point the presence of shear bands formed by secondary voids aligned with the stress field.

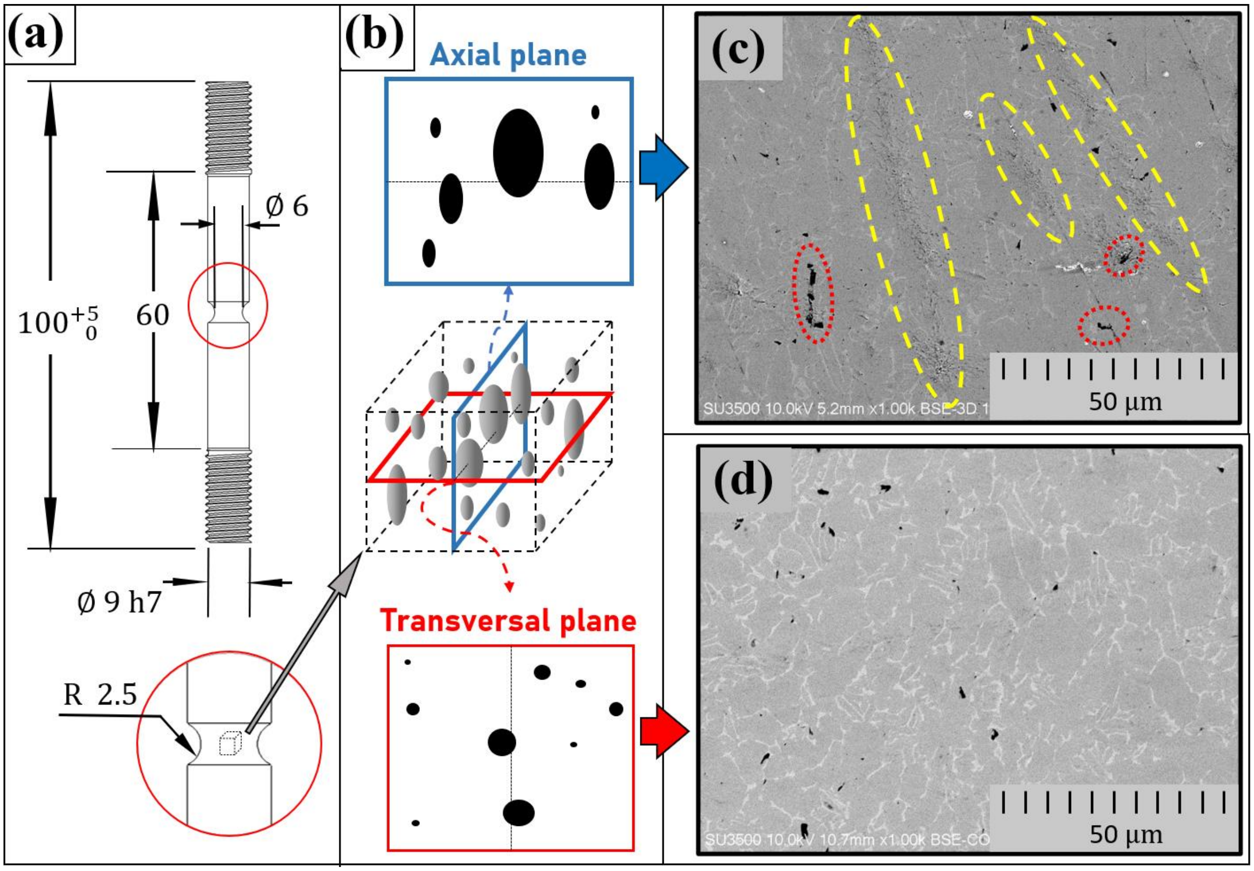

Figure 3. **(a)** Geometry of Ti–6Al–4V notches bar specimen submitted to a near-fracture tensile test. Dimensions in millimeters. **(b)** Effect of the deformation field over the shape and size of cavities located at the SEM sampling zones. **(c)** and **(d)** are representative SEM images from the axial and transversal notch planes respectively.

The digital post-processing of SEM images captured at different sampling zones (A, B and C) within the axial and transversal planes allowed to obtain a mapping of the apparent porosity ratio, presented in Figure 4.

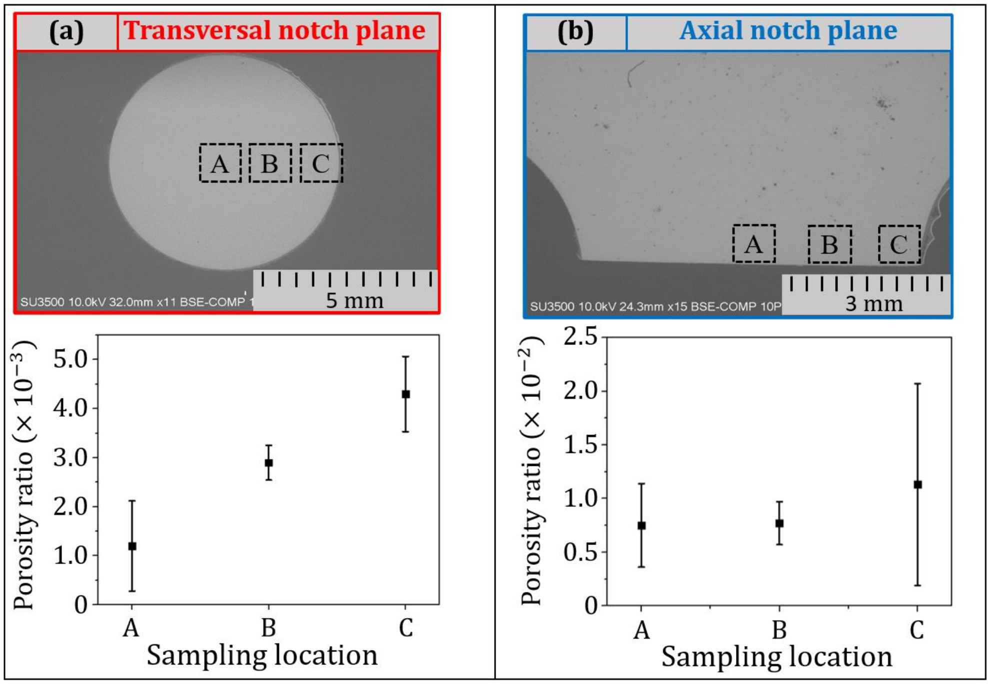

Figure 4. SEM images of transversal **(a)** and axial **(b)** notch planes and respective localized apparent porosity ratio analyses in sampling locations A, B and C for each notch plane sample.

3.2. Identification of damage parameters

3.2.1. Growth parameters

Following the void growth model presented in Equation 5, the only essential parameter to be identified is the initial porosity ratio f_0 of the material. Identified throughout SEM imaging of pristine samples of this particular batch of Ti–6Al–4V alloy, the authors from Verleysen & Peirs reported an $f_0=3\times10^{-5}$,[45] while the authors from Tuninetti et.al. reported an $f_0=8\times10^{-5}$.[14] In consequence, an initial porosity ratio of $f_0=5\times10^{-5}$ was selected as an in-between value for further FE simulations.

3.2.2. Nucleation parameters

The identification of the nucleation parameters was performed throughout a direct identification procedure. Prior to the onset of coalescence, the porosity ratio due to growth is negligible in comparison to the porosity ratio due to nucleation. With this in mind, the nucleation model parameters (F_N, S_N and ϵ_N) were directly identified by fitting the numerical nucleation model curve from Equation 6 to the experimental data given by Lecarme et.al.[31], resulting in F_N=0.016, S_N=0.12 and ϵ_N=0.375. The geometry of the Ti–6Al–4V notched bar submitted to the in-situ X-ray tomography procedure along with subsequent graph exhibiting the experimentally determined total porosity ratio in conjunction with the resultant curve of the identified numerical nucleation model are illustrated in Figure 5.

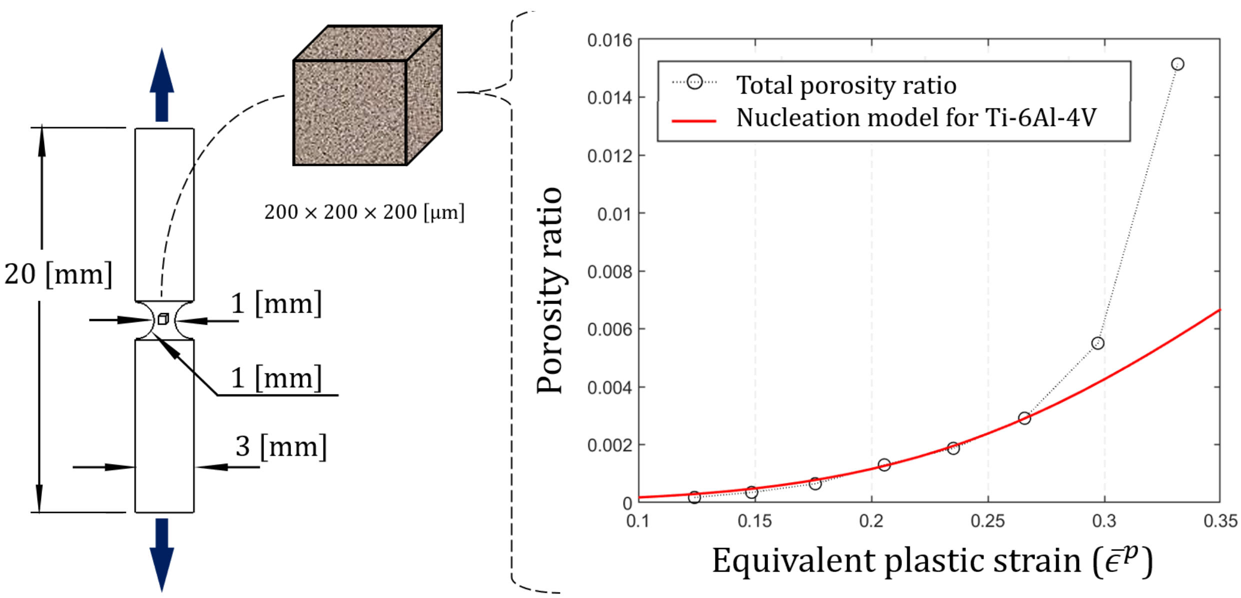

Figure 5. Illustration of X-ray tomography procedure, measured porosity ratio and proposed nucleation porosity ratio for Ti–6Al–4V.

3.2.3. Coalescence parameters

The abrupt divergence between experimental data and numerical model observed in Figure 5 is attributed to the onset of coalescence. Hence, the critical porosity ratio of the material is set to $f_{\mathrm{cr}} = 0.003$. Subsequently, by fixing the fracture porosity ratio at f_F=0.2 in link with the research findings form Verleysen & Peirs,[45] it was possible to execute an inverse identification procedure with the objective of finding the ultimate porosity ratio. Following this procedure, it was found that the ultimate porosity ratio for this material is f_U=0.4.

3.2.4. Tvergaard & Needleman parameters

The parameters introduced by Tvergaard & Needleman (q_1, q_2 and q_3) are directly identified by taking into consideration the mathematical relations given in Ref.[41], while setting q_2=1.0 as proposed in previous research. This is:

$$\begin{cases} q_1 = \frac{1}{f_{\mathrm{U}}} \\ q_3 = (q_1)^2 \end{cases} \tag{9}$$

Taking into consideration the coalescence parameters already found, the parameters presented in Equation 9 are q_1=2.50 and q_3=6.25.

As a result of the analyses and procedures described above, the whole set of parameters and constants for modeling the damage evolution of Ti–6Al–4V using the SC11—TN extended micromechanics damage model are summarized in Table 2.

Table 2. Parameters for modeling the growth, nucleation and coalescence of voids in Ti–6Al–4V through the SC11—TN extended damage law.

Initial porosity ratio f_0=5×10^{-5}		
Nucleation model parameters (Equation 6)		
F_N	S_N	ϵ_N
0.016	0.12	0.375
Coalescence model parameters (Equation 7)		
f_{cr}	f_U	f_F
0.003	0.40	0.20
Tvergaard & Needleman parameters		
q_1	q_2	q_3
2.50	1.00	6.25

4. Validation of micromechanical model

4.1. Mesh and boundary conditions

The FE meshes of the notched and smooth bar specimens geometries were designed with the GMSH software.[46] Hexahedral 3D brick elements of the type BWD3D were used, each one containing 8 nodes, one point of integration and 24 degrees of freedom (DOF).[47] Based on the results of a mesh sensitivity analysis, the optimal number of elements found for geometries A and B was 21870, while for geometry C (smooth) 11421 elements were used. The mesh and boundary conditions for all the notched bar specimens is presented in Figure 6 (b). A continuous measurement of the displacement in the tensile test FE simulations similar with the experimental extensometer measurement technique is achieved by measuring the current displacement distance at the points where the extensometer clip was positioned (Figure 6 (a)).

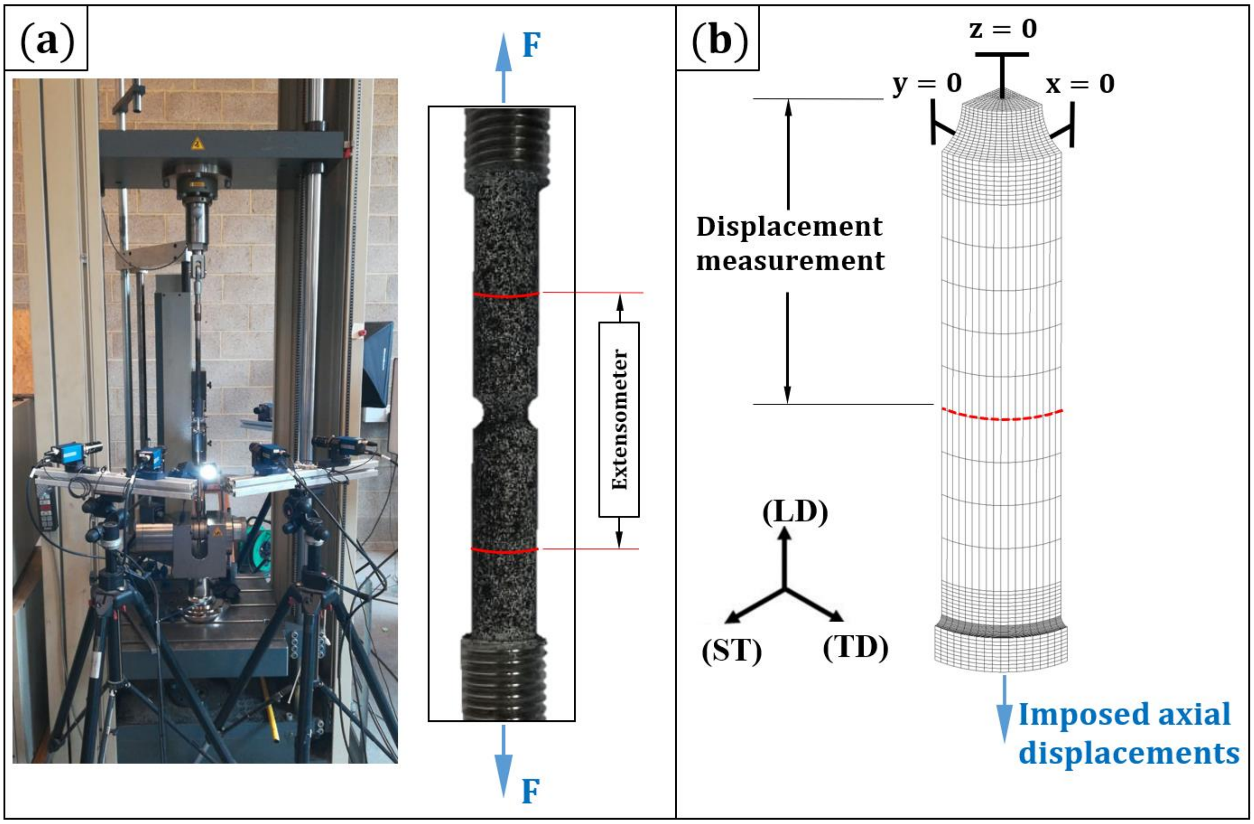

Figure 6. (a) Experimental mounting of Ti–6Al–4V notched bar specimen and DIC system on universal testing machine. **(b)** Mesh and boundary conditions of R5 mm notched bar specimen, applied in all notched and smooth bar tensile tests FE simulations.

4.2. Validation of SC11—TN for Ti–6Al–4V

In the framework of this validation procedure, and with the objective of obtaining a more complete depiction of the SC11—TN damage law prediction capabilities, the validated CPB06 orthotropic asymmetric yield criterion is also considered. Note that the implementation of SC11—TN was checked as when damage is de-activated the predictions exactly recovered CPB06 law results.

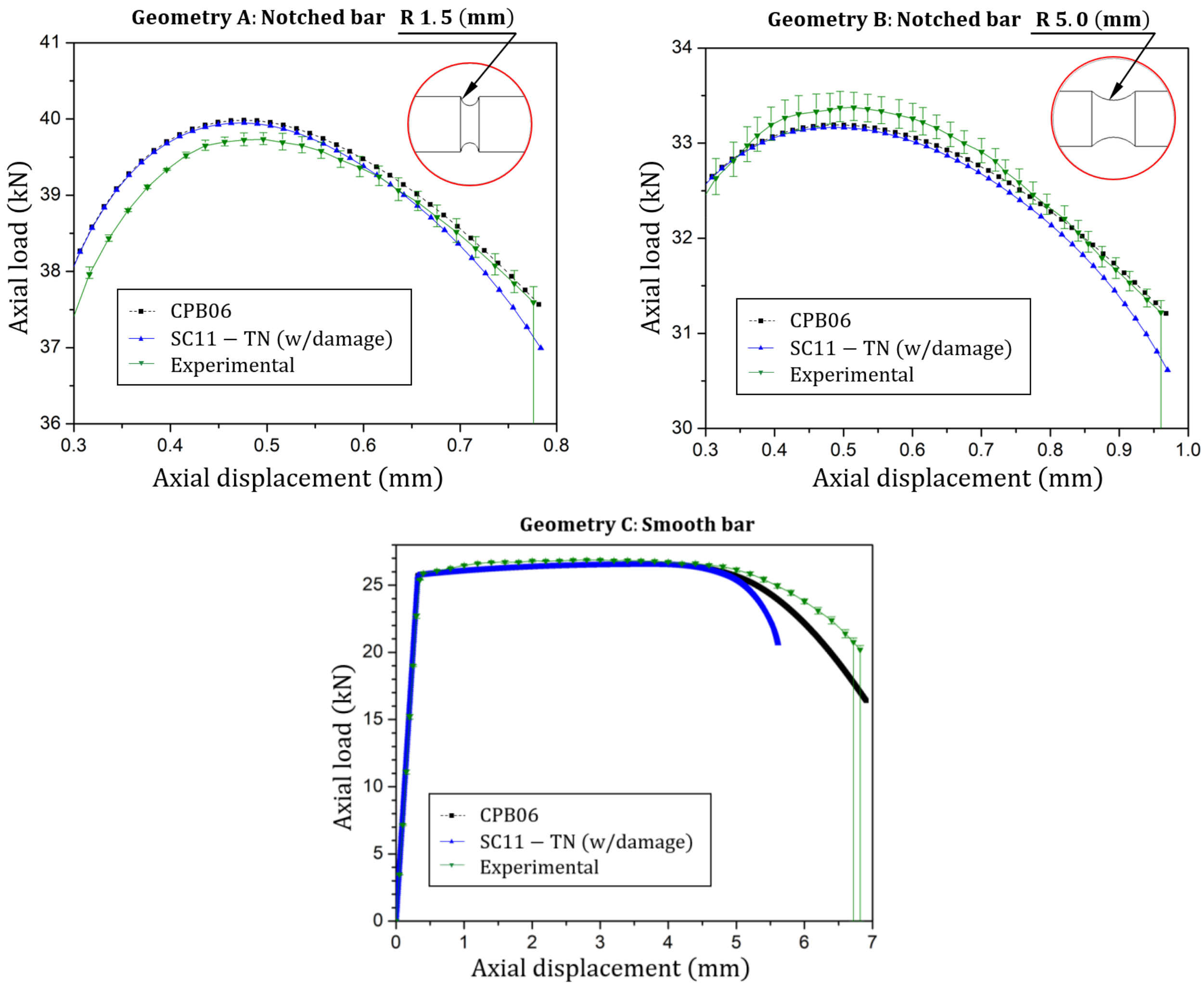

Figure 7. Superposition of load-displacement curves resultant from experimental and FE simulation tensile tests simulation of geometries **A**, **B** and **C**.

The load-displacement results of SC11—TN model shown in Figure 7 reveal that the load prediction capabilities of this new damage law are in reasonable agreement with the experimental results, however the predicted softening is too high. This result is consistent with the fact that the used elasto-plastic set of parameters was identified without damage. The effect of the addition of damage is evidenced in the decrease of the SC11—TN predicted loads. This decrease is directly related to the presence and continuous increment of the total porosity ratio. However, as near-fracture strains are reached, the huge raise of total porosity ratio leads to a too high softening of the predicted axial load, i.e., it predicts a lower fracture load. This prediction disagreement is highly noticeable in the smooth bar load-displacement curves, where the particularly high strains develop in high porosity ratio values. Clearly additional identification should be performed to conclude about the nucleation and coalescence extension interest about force prediction.

4.3 Damage evolution analysis

The geometry **A** (R 1.5 mm) is recognized to have the highest average triaxiality among the ones considered in this research. Therefore, the evolution of triaxiality and total porosity ratio along the radial ST direction of this R 1.5 mm notched bar is analyzed in Figure 8.

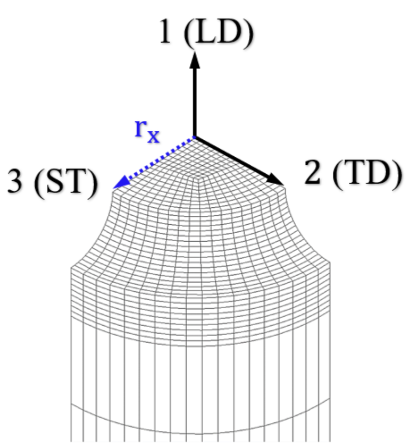

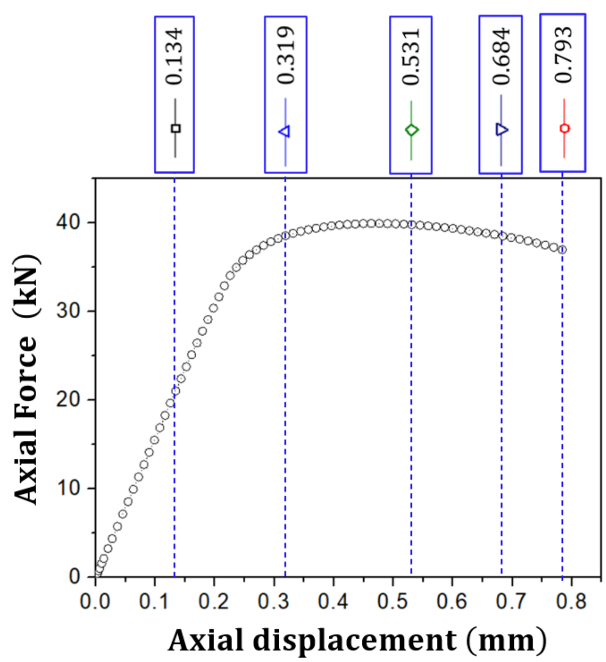

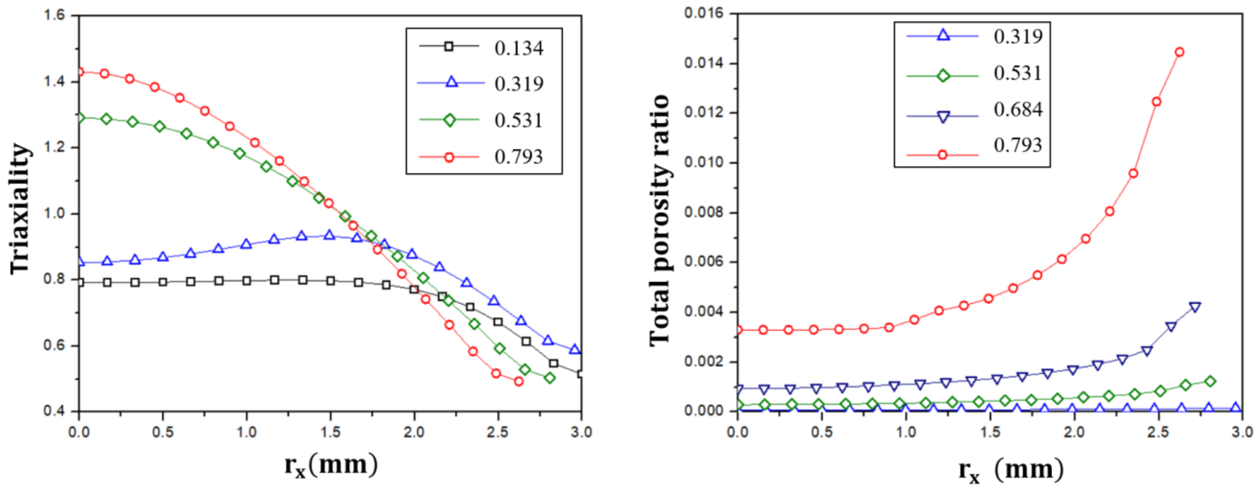

Figure 8. Evolution of triaxiality and total porosity ratio along large and near-fracture displacements (0,13, 0.32, 0.53, 0.68 and 0.79 mm) over the R 1.5 mm Ti–6Al–4V notched bar specimen.

As seen in Figure 8, the deformation of the notch shape geometry along the tensile test affects the triaxiality in such way that the location of its maximum zone starts near the surface edge of the notch neck plane and is displaced towards the central LD axis. However, this change is not reflected in the measurement of the total porosity ratio of the radial node configuration. The fracture configuration of damage and damage related state variables of this particular notched bar, presented in Figure **9**, show that the coalescence of voids plays a much more significant role in the overall total porosity ratio evolution. This behavior is also observed in the analyses of the fracture-state variables for the R 5.0 mm notched bar and smooth bar specimens, shown respectively in Figure 10 and Figure 11.

In Figure **9**, Figure 10 and Figure 11, the implemented growth and nucleation analytical formulations (Equation 5 and 6 respectively) are used for calculating their respective contributions to the total porosity ratio. The coalescence contribution is calculated by subtracting the growth and nucleation contributions with the total porosity ratio. This is:

$$f_c = D - f_g - f_n \tag{9}$$

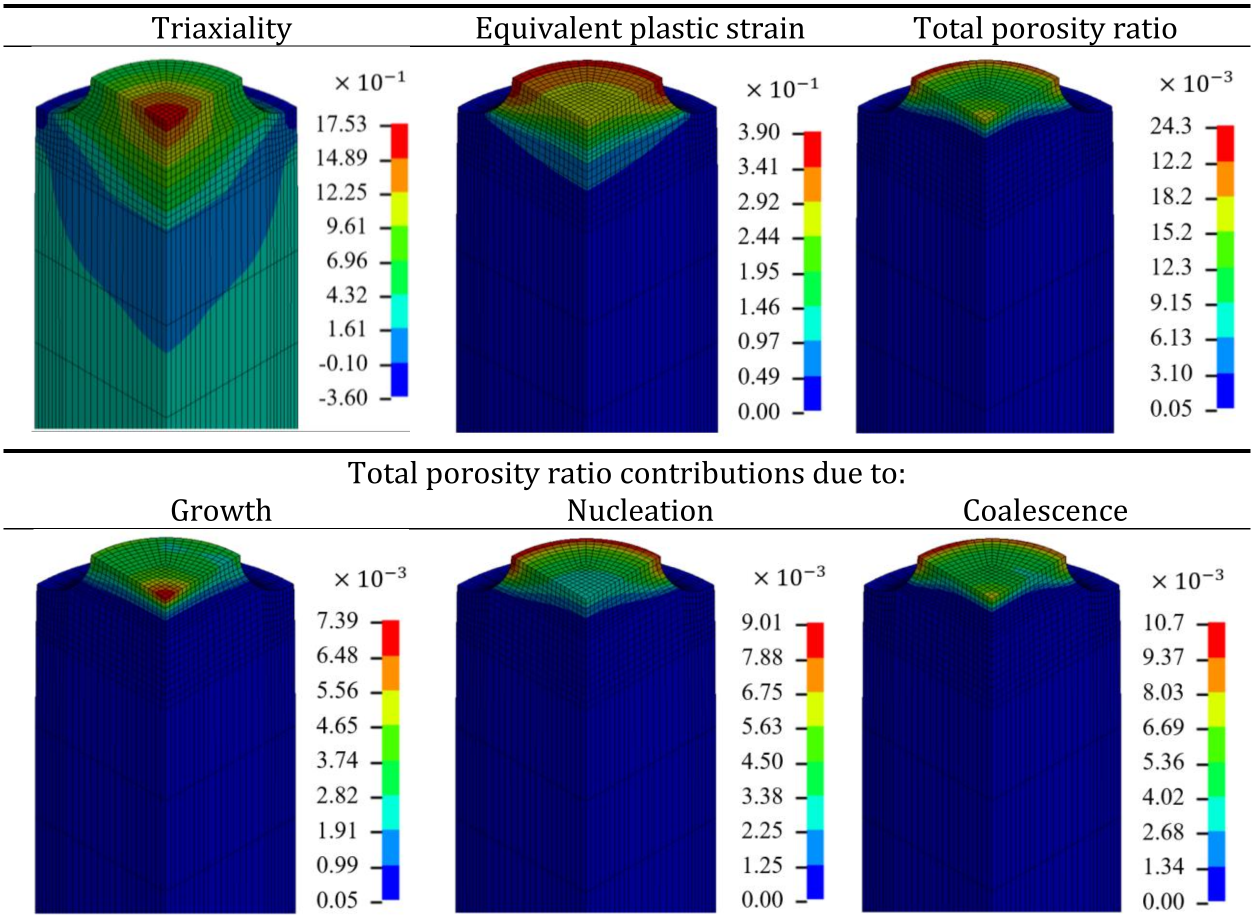

Figure 9**.** Compilation of damage and damage related state variables in R 1.5 mm notched bar specimen of Ti–6Al–4V at its fracture state configuration.

Triaxiality	Equivalent plastic strain	Total porosity ratio

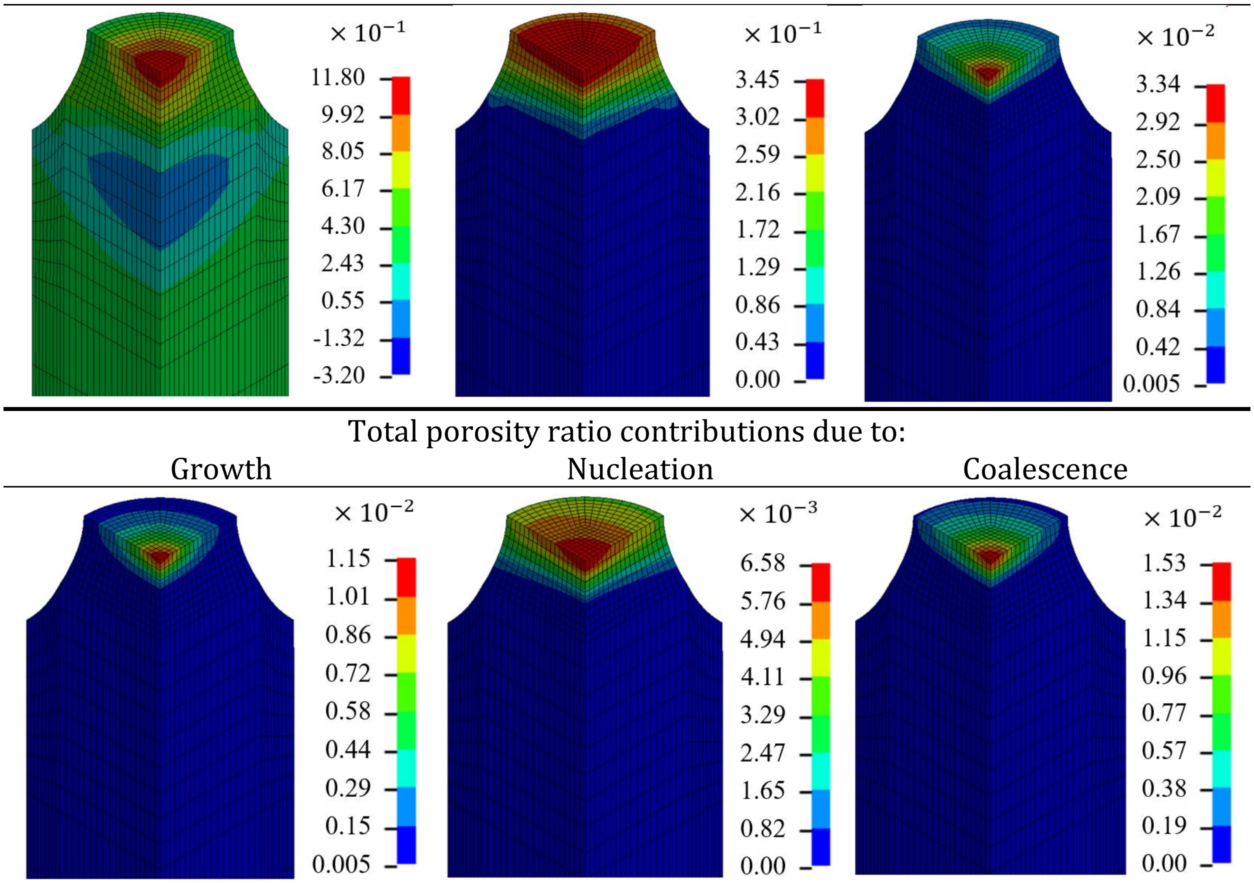

Figure 10. Compilation of damage and damage related state variables in R 5.0 mm notched bar specimen of Ti–6Al–4V at its fracture state configuration.

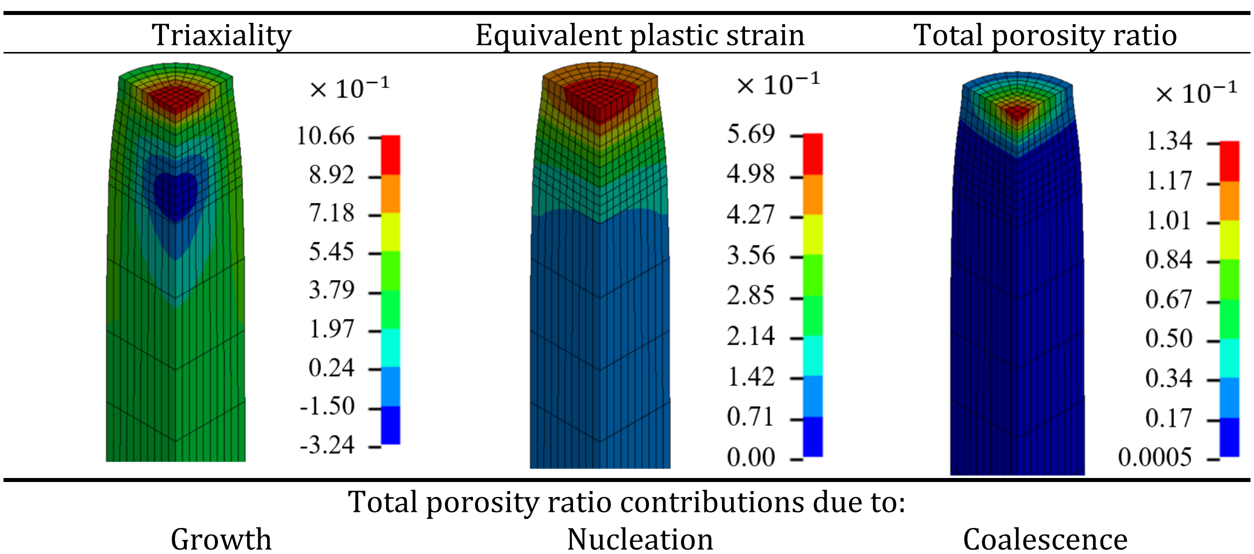

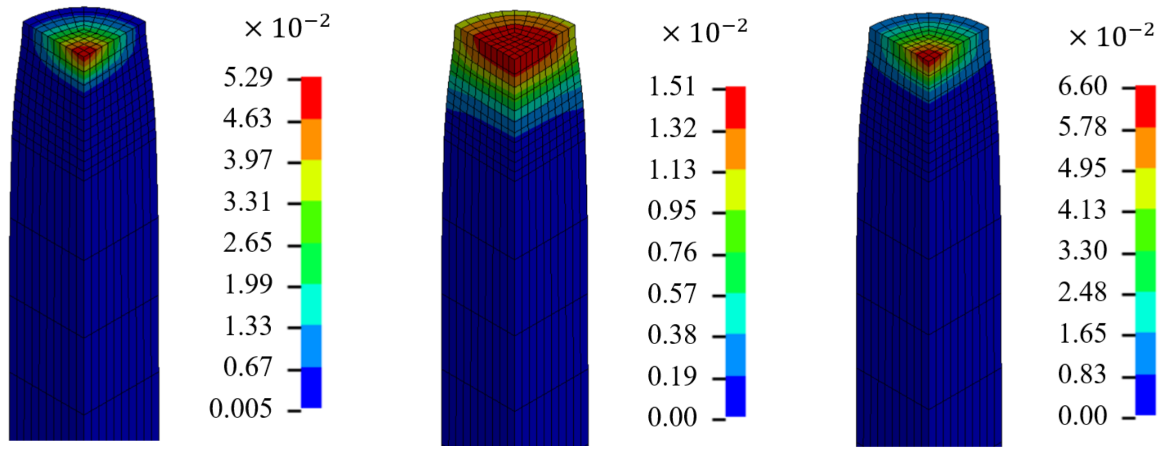

Figure 11. Compilation of damage and damage related state variables in smooth bar specimen of Ti–6Al–4V at its fracture state configuration.

The analysis of damage and damage related state variables in fracture configuration for all the geometries presented in Figure **9**, Figure 10 and Figure 11 show that the critical zones, where the onset of fracture is predicted, are directly related to the zones where the maximum equivalent plastic strain values are reached. In particular, it is observed in the smooth bar analysis shown in Figure 11 the presence of extremely high values of total porosity ratio and equivalent plastic strain. This concentration of total porosity at the center of the notch plane in the cylindrical smooth bar is in good agreement with experimentally observed fractography images of tensile fracture of Ti–6Al–4V cylindrical smooth bars.[44,45] A compilation of the maximum values of the reported damage and damage relates state variables at fracture configuration is given in Table 3.

Table 3. Maximum values of damage and damage related state variables at fracture configuration for the three assessed Ti–6Al–4V bar geometries.

Geometry	Triaxiality	$\bar{\epsilon}^p$	D	f_g	f_n	f_c

A	R 1.5 mm	1.75	0.39	0.024	0.007	0.009	0.001
B	R 5.0 mm	1.18	0.34	0.033	0.011	0.007	0.015
C	Smooth	1.06	0.57	0.134	0.053	0.015	0.066

These results are consistent with the selected analytical formulations for modeling growth, nucleation and coalescence of voids. The trace of plastic strain rate tensor $\mathbf{d^p}$ and the triaxiality play significant roles in the growth of voids (Equation 5). Moreover, nucleation and coalescence of voids respectively expressed in Equation 6 and 7 are explicitly dependent of the equivalent plastic strain $\bar{\epsilon}^p$. The numerical results of this identified SC11—TN damage model for the Ti–6Al–4V confirm that high positive triaxiality geometries exhibit large increment of initial voids size, while specimens reaching large strains such as the smooth bar will be highly affected by nucleation and coalescence of voids.

The prediction capabilities of any model rely in the accuracy and the reliability of the characterization procedure carried out for its material parameters identification. In this particular case, the parameters of the Voce's isotropic hardening law applied to the damage model were previously identified in Tuninetti et al.[14] considering post-necking strains until a true strain of 0.2. Improvements for higher accuracy of the near fracture load with the SC11—TN damage model for this alloy should be done using neural networks or more classical optimization schema.[12,48] Moreover, the implementation of an ultra-high speed DIC will enable the detection of deformations and microcracks formed in the surface of the analyzed specimen, hence enabling the analysis of the formation of microcracks on the outer radial section of the notch as predicted in Figure 9.

5. Conclusions

In this work, the results of a new SC11—TN extended coupled damage law was implemented in the FE software Lagamine, and validated for positive triaxialities considering three tensile tests with three different geometries (two notched and one smooth Ti–6Al–4V bar specimens) were considered. The damage characterization was addressed by measurements of the continuous total porosity ratio by means of in-situ X-ray tomography data and near-fracture total porosity ratio throughout SEM imaging technique. The resultant load-displacement and damage related state variables analyses along this variety of triaxialities related to the notch geometries allowed to conclude that:

- The SC11—TN extended continuum micromechanics damage law has proven to be suitable for modeling the elastoplastic and damage behavior of Ti–6Al–4V alloy, predicting axial load values reasonably within the error bars of correspondent experimental tests.
- The tensile finite element simulations results allowed to numerically analyze the identified set of damage parameters. Furthermore, the localization of damage within the critical zone of the Ti–6Al–4V smooth bar specimen is in good agreement with experimentally observed fracture analysis.

These results open new doors for further research in material modeling and ductile fracture mechanics. In order to enhance the prediction ability of the SC11—TN damage law, further work must be focused on performing a new identification procedure of isotropic hardening and damage models in one step, acknowledging near-fracture strains.

Acknowledgements

This work was funded by the National Agency for Research and Development (ANID) Fondecyt 11170002 and the cooperation agreement WBI/AGCID SUB2019/419031 (DIE19-0005). As research director of FRS-FNRS, A.M. Habraken thanks the Belgian Scientific Research Fund FNRS for financial support. The authors also acknowledge FONDEQUIP EQM130014.

References

1. Pineau A, Pardoen T. 2.06 - Failure of Metals. *Compr Struct Integr* 2007; 2: 684–797.
2. Seidenfuss M, Linse T. *Recent Trends in Fracture and Damage Mechanics*. Cham: Springer International Publishing. Epub ahead of print 2016. DOI: 10.1007/978-3-319-21467-2.
3. Li H, Fu M. Damage Evolution and Ductile Fracture. In: *Deformation-Based Processing of Materials*. Elsevier, pp. 85–136.
4. Yildiz RA, Yilmaz S. Experimental Investigation of GTN model parameters of 6061 Al alloy. *Eur J Mech A/Solids* 2020; 83: 104040.
5. Duchêne L, Habraken AM. Analysis of the sensitivity of FEM predictions to numerical parameters in deep drawing simulations. *Eur J Mech - A/Solids* 2005; 24: 614–629.
6. Tuninetti V, Yuan S, Gilles G, et al. Modeling the ductile fracture and the plastic anisotropy of DC01 steel at room temperature and low strain rates. *J Phys Conf Ser* 2016; 734: 032075.
7. Duchêne L, Ben Bettaieb A, Tuninetti V, et al. Numerical Modeling and Digital Image Correlation Strain Measurements of Coated Metal Sheets Submitted to Large Bending Deformation. *Key Eng Mater* 2013; 554–557: 2424–2431.
8. Guzmán CF, Yuan S, Duchêne L, et al. Damage prediction in single point incremental forming using an extended Gurson model. *Int J Solids Struct* 2018; 151: 45–56.
9. Wagener H-W, Hosse-Hartmann J, Friz R. Deep Drawing and Impact Extrusion of Magnesium Alloys at Room Temparature. *Adv Eng Mater* 2003; 5: 237–242.
10. Cazacu O, Plunkett B, Barlat F. Orthotropic yield criterion for hexagonal closed packed metals. *Int J Plast* 2006; 22: 1171–1194.
11. Cazacu O, Revil-Baudard B, Chandola N. *Plasticity-Damage Couplings: From Single*

Crystal to Polycrystalline Materials, http://link.springer.com/10.1007/978-3-319-92922-4 (2019).

12. Tuninetti V, Habraken AM. Impact of anisotropy and viscosity to model the mechanical behavior of Ti–6Al–4V alloy. *Mater Sci Eng A* 2014; 605: 39–50.

13. Tuninetti V, Gilles G, Milis O, et al. Anisotropy and tension–compression asymmetry modeling of the room temperature plastic response of Ti–6Al–4V. *Int J Plast* 2015; 67: 53–68.

14. Tuninetti V, Gilles G, Flores P, et al. Impact of distortional hardening and the strength differential effect on the prediction of large deformation behavior of the Ti6Al4V alloy. *Meccanica* 2019; 54: 1823–1840.

15. Rym Harbaoui, Olfa Daghfas, Amna Znaidi, et al. Mechanical behavior of materials with a compact hexagonal structure obtained by an advanced identification strategy of HCP material, AZ31B-H24. *Frat ed Integrità Strutt* 2020; 14: 295–305.

16. Rym H, Olfa D, Amna Z. Strategy for identification of HCP structure materials: study of Ti–6Al–4V under tensile and compressive load conditions. *Arch Appl Mech* 2020; 90: 1685–1703.

17. Stewart JB, Cazacu O. Analytical yield criterion for an anisotropic material containing spherical voids and exhibiting tension–compression asymmetry. *Int J Solids Struct* 2011; 48: 357–373.

18. Poondla N, Srivatsan TS, Patnaik A, et al. A study of the microstructure and hardness of two titanium alloys: Commercially pure and Ti-6Al-4V. *J Alloys Compd* 2009; 486: 162–167.

19. Bettaieb M Ben, Van Hoof T, Minnebo H, et al. Micromechanics-Based Damage Analysis of Fracture in Ti5553 Alloy with Application to Bolted Sectors. *J Mater Eng Perform* 2015; 24: 1262–1278.

20. Montgomery JS, Wells MGH. Titanium armor applications in combat vehicles. *JOM* 2001; 53: 29–32.

21. Cazacu O. Development of a Multi-Scale Methodology for Prediction of the Macroscopic Anisotropic Stress-Strain Response of Textured Metals under Dynamic Loading. *US Airf Res Lab* 2009; 1–69.

22. Castellanos SD, Cavaleiro AJ, Jesus AMPD, et al. Machinability of titanium aluminides: A review. *Proc Inst Mech Eng Part L J Mater Des Appl* 2019; 233: 426–451.

23. Sarao TPS, Singh H, Singh H. Enhancing Biocompatibility and Corrosion Resistance of Ti-6Al-4V Alloy by Surface Modification Route. *J Therm Spray Technol* 2018; 27: 1388–1400.

24. Zhou YL, Niinomi M, Akahori T, et al. Corrosion resistance and biocompatibility of Ti–Ta alloys for biomedical applications. *Mater Sci Eng A* 2005; 398: 28–36.

25. Mcandrew AR, Colegrove PA, Bühr C, et al. Progress in Materials Science A literature

review of Ti-6Al-4V linear friction welding. *Prog Mater Sci* 2018; 92: 225–257.

26. Zhang M, Zhang J, McDowell DL. Microstructure-based crystal plasticity modeling of cyclic deformation of Ti-6Al-4V. *Int J Plast* 2007; 23: 1328–1348.

27. Tuninetti V, Flores P, Valenzuela M, et al. Experimental characterization of the compressive mechanical behaviour of Ti6Al4V alloy at constant strain rates over the full elastoplastic range. *Int J Mater Form* 2020; 13: 709–724.

28. Tuninetti V, Jaramillo AF, Riu G, et al. Experimental Correlation of Mechanical Properties of the Ti-6Al-4V Alloy at Different Length Scales. *Metals (Basel)* 2021; 11: 104.

29. Xue Q, Meyers MA, Nesterenko VF. Self-organization of shear bands in titanium and Ti-6Al-4V alloy. *Acta Mater* 2002; 50: 575–596.

30. Boehlert CJ, Cowen CJ, Tamirisakandala S, et al. In situ scanning electron microscopy observations of tensile deformation in a boron-modified Ti-6Al-4V alloy. *Scr Mater* 2006; 55: 465–468.

31. Lecarme L, Maire E, Kumar A, et al. Heterogenous void growth revealed by in situ 3-D X-ray microtomography using automatic cavity tracking. *Acta Mater* 2014; 63: 130–139.

32. Zhang XC, Zhong F, Shao JB, et al. Failure mechanism and mode of Ti-6Al-4V alloy under uniaxial tensile loading: Experiments and micromechanical modeling. *Mater Sci Eng A* 2016; 676: 536–545.

33. Tan J, Lu L, Li HY, et al. Anisotropic deformation and damage of dual-phase Ti-6Al-4V under high strain rate loading. *Mater Sci Eng A* 2019; 742: 532–539.

34. Rice JR, Tracey DM. On the ductile enlargement of voids in triaxial stress fields. *J Mech Phys Solids* 1969; 17: 201–217.

35. Gurson AL. Continuum theory of ductile rupture by void nucleation and growth. *J Eng Mater Technol* 1977; 99: 2–15.

36. Margolin H, Mahajan Y. Void formation, void growth and tensile fracture in Ti-6AI-4V. *Metall Trans A* 1978; 9: 781–791.

37. Tvergaard V. Influence of voids on shear band instabilities under plane strain conditions. *Int J Fract* 1981; 17: 389–407.

38. Becker R, Needleman A, Richmond O, et al. Void growth and failure in notched bars. *J Mech Phys Solids* 1988; 36: 317–351.

39. Perrin G, Leblond JB. Analytical study of a hollow sphere made of plastic porous material and subjected to hydrostatic tension-application to some problems in ductile fracture of metals. *Int J Plast* 1990; 6: 677–699.

40. Brünig M, Gerke S, Schmidt M. Damage and failure at negative stress triaxialities: Experiments, modeling and numerical simulations. *Int J Plast* 2018; 102: 70–82.

41. Tvergaard V, Needleman A. Analysis of the cup-cone fracture in a round tensile bar. *Acta Metall* 1984; 32: 157–169.

42. Armstrong PJ, Frederick CO. A Mathematical Representation of the Multi Axial Bauschinger Effect. *Mater High Temp* 1966; 24: 1–26.

43. Guzmán CF, Tuninetti V, Gilles G, et al. Assessment of Damage and Anisotropic Plasticity Models to Predict Ti-6Al-4V Behavior. *Key Eng Mater* 2015; 651–653: 575–580.

44. Lecarme L. *Viscoplasticity, damage, and fracture of Ti-6Al-4V*. 2013.

45. Verleysen P, Peirs J. Quasi-static and high strain rate fracture behaviour of Ti6Al4V. *Int J Impact Eng* 2017; 108: 370–388.

46. Geuzaine C, Remacle J-F. Gmsh: A 3-D finite element mesh generator with built-in pre- and post-processing facilities. *Int J Numer Methods Eng* 2009; 79: 1309–1331.

47. Zhu YY, Cescotto S. Unified and mixed formulation of the 8-node hexahedral elements by assumed strain method. *Comput Methods Appl Mech Eng* 1996; 129: 177–209.

48. Marouani H, Aguir H. Identification of material parameters of the Gurson–Tvergaard–Needleman damage law by combined experimental, numerical sheet metal blanking techniques and artificial neural networks approach. *Int J Mater Form* 2012; 5: 147–155.